

Lawrence Berkeley National Laboratory

Lawrence Berkeley National Laboratory

Title

Comparative soil CO2 flux measurements and geostatistical estimation methods on masaya volcano, nicaragua

Permalink

<https://escholarship.org/uc/item/8tb2v75h>

Authors

Lewicki, J.L.
Bergfeld, D.
Cardellini, C.
et al.

Publication Date

2004-04-27

Peer reviewed

Comparative soil CO₂ flux measurements and geostatistical estimation methods on Masaya volcano, Nicaragua

J. L. Lewicki¹, D. Bergfeld², C. Cardellini³, G. Chiodini⁴, D. Granieri⁴, N. Varley⁵, and C. Werner⁶

Short title: COMPARATIVE SOIL CO₂ FLUX MEASUREMENTS

¹Earth Sciences Division, Lawrence Berkeley National Laboratory, Berkeley, California, USA.

²U.S. Geological Survey, Menlo Park, California, USA.

³Dipartimento di Scienze della Terra, Università di Perugia, Perugia, Italy.

⁴Osservatorio Vesuviano, Istituto Nazionale di Geofisica e Vulcanologia, Napoli, Italy.

⁵Facultad de Ciencias, Universidad de Colima, Colima, Mexico.

⁶Institute of Geological and Nuclear Sciences, Taupo, New Zealand.

Abstract. We present a comparative study of soil CO₂ flux (F_{CO_2}) measured by five groups (Groups 1-5) at the IAVCEI-CCVG Eighth Workshop on Volcanic Gases on Masaya volcano, Nicaragua. Groups 1-5 measured F_{CO_2} using the accumulation chamber method at 5-m spacing within a 900 m² grid during a morning (AM) period. These measurements were repeated by Groups 1-3 during an afternoon (PM) period. All measured F_{CO_2} ranged from 218 to 14,719 g m⁻²d⁻¹. Arithmetic means and associated CO₂ emission rate estimates for the AM data sets varied between groups by $\pm 22\%$. The variability of the five measurements made at each grid point ranged from ± 5 to 167% and increased with the arithmetic mean. Based on a comparison of measurements made by Groups 1-3 during AM and PM times, this variability is likely due in large part to natural temporal variability of gas flow, rather than to measurement error. We compared six geostatistical methods (arithmetic and minimum variance unbiased estimator means of uninterpolated data, and arithmetic means of data interpolated by the multiquadric radial basis function, ordinary kriging, multi-Gaussian kriging, and sequential Gaussian simulation methods) to estimate the mean and associated CO₂ emission rate of one data set and to map the spatial F_{CO_2} distribution. While the CO₂ emission rates estimated using the different techniques only varied by $\pm 1.1\%$, the F_{CO_2} maps showed important differences. We suggest that the sequential Gaussian simulation method yields the most realistic representation of the spatial distribution of F_{CO_2} and is most appropriate for volcano monitoring applications.

Introduction

Measurement of soil CO₂ flux (F_{CO_2}) and its natural spatial and temporal variability in volcanic, geothermal, and metamorphic (VGM) environments has important implications for volcano monitoring, geothermal exploration, delineation of fault and fracture zones, and estimation of the contribution of CO₂ from VGM sources to the global carbon cycle. Numerous studies have been conducted during the past decade to measure F_{CO_2} , map its areal distribution, and estimate total CO₂ emission rates from VGM areas of interest [e.g., *Farrar et al.*, 1995; *Giammanco et al.*, 1997; *Chiodini et al.*, 1998; *Werner et al.*, 2000; *Gerlach et al.*, 2001; *Bergfeld et al.*, 2001; *Gerlach et al.*, 2001; *Salazar et al.*, 2001; *Rogie et al.*, 2001; *Chiodini et al.*, 2001; *Lewicki et al.*, 2003a; *Cardellini et al.*, 2003]. However, these investigations have applied a wide range of measurement and statistical methodologies to accomplish these goals. Importantly, the choice of these methodologies may largely affect individual F_{CO_2} measurements and characterization of their natural spatial and temporal variability, the total CO₂ emission rate estimated for a given area, and the ability to assess the uncertainty associated with this estimate.

The primary sources of variability of individual F_{CO_2} measurements in VGM systems are measurement methodology and the natural spatial and temporal variability of subsurface and surface parameters that influence gas flow. Natural changes in the system may include spatial and temporal variations in the physical properties of the medium (e.g., porosity, permeability), biogenic respiration, meteorological parameters

(e.g., atmospheric pressure, temperature, and wind speed and direction), and the deep CO_2 source.

Most investigations of VGM F_{CO_2} use accumulation chamber methods for F_{CO_2} measurement. While the use of an accumulation chamber with an infrared gas analyzer provides a simple and rapid measurement, placement of the chamber on the soil can alter the F_{CO_2} from its natural undisturbed rate. For example, chambers can disturb the F_{CO_2} by altering the air pressure within the chamber, changing the CO_2 concentration gradient across the soil-air interface, diverting gas flow around the chamber, and causing a build-up of water vapor within the chamber [e.g., *Welles et al.*, 2001; *Evans et al.*, 2001]. In addition, to ensure a seal between the chamber and the soil surface that minimizes inflow of atmospheric air during the measurement, it may be necessary to disturb the soil, either by direct placement of the chamber on the soil or by insertion of a "collar" into the soil on which the chamber rests. This alteration of soil physical properties also has the potential to change the natural F_{CO_2} [e.g., *Gerlach et al.*, 2001]. While techniques were developed to reduce the effects of the chamber presence on the natural F_{CO_2} , these effects may be difficult to prevent entirely and should be considered in the interpretation of measured F_{CO_2} . Together, natural and measurement related effects will lead to variability of measured values within a given data set and between different researchers data sets. While the researcher is generally interested to characterize the natural variability of F_{CO_2} , it can be difficult to separate this from the variability introduced by the F_{CO_2} measurement technique. Although laboratory tests on imposed CO_2 fluxes using multiple measurement techniques have been described

[*Evans et al.*, 2001], comparative measurements of F_{CO_2} in VGM environments have not yet been presented in the literature.

Maps of F_{CO_2} may be produced using a variety of methods. If F_{CO_2} measurements are made at both evenly and tightly spaced intervals along a grid, an uninterpolated map can be constructed representing the spatial distribution of F_{CO_2} . However, it is often the case that F_{CO_2} measurements are made at widely and/or unevenly spaced intervals within an area. In this case, statistical methods must be employed to interpolate F_{CO_2} values at unsampled locations. This has been accomplished most commonly by kriging methods [e.g., *Salazar et al.*, 2001; *Rogie et al.*, 2001; *Gerlach et al.*, 2001] and, more recently, by a sequential Gaussian simulation technique [*Cardellini et al.*, 2003].

The primary techniques used to estimate the total CO₂ emission rate from a given area are (1) multiplying the arithmetic mean of measured F_{CO_2} values by the surveyed area, (2) multiplying the mean of F_{CO_2} values estimated by minimum variance unbiased estimators [*Finney*, 1941; *Sichel*, 1952] by the surveyed area, (3) applying volume and area integration algorithms to an interpolated F_{CO_2} grid, (4) applying a graphical statistical approach (GSA) described by *Chiodini et al.* [1998], or (5) applying sequential Gaussian simulations [*Deutsch and Journel*, 1998; *Cardellini et al.*, 2003]. While the choice of these methods has the potential to significantly affect the resulting F_{CO_2} map and the estimated CO₂ emission rate, to date, the range of methods have not been applied to a single VGM F_{CO_2} data set for comparison.

The Eighth Field Workshop on Volcanic Gases (25 March to 2 April, 2003), sponsored by the Commission on the Chemistry of Volcanic Gases (CCVG) and

the International Association of Volcanology and Chemistry of the Earth's Interior (IAVCEI) [Wardell *et al.*, 2003] provided the unique opportunity for multiple groups of researchers to make comparative F_{CO_2} measurements in an area of elevated diffuse degassing on the flanks of Masaya volcano, Nicaragua (Figure 1). Here, we compare the measured F_{CO_2} data sets, present a range of interpolation and estimation methods applied previously in VGM studies, and apply these methods to map F_{CO_2} and estimate total CO₂ emissions from the study area. Furthermore, we discuss the potential sources of discrepancies between the different F_{CO_2} measurements and estimated CO₂ emission rates and implications for future F_{CO_2} studies in VGM areas.

Figure 1.

Study Area

The study area is located adjacent to Comalito cinder cone on the northeast flanks of Masaya volcano, Nicaragua (Figure 1). Masaya is a basaltic shield volcano that has displayed cycles of voluminous degassing, the most recent of which began in 1993 and continues from the active Santiago crater [e.g., Delmelle *et al.*, 1999]. Numerous plume degassing studies have been conducted at Masaya [e.g., Stoiber *et al.*, 1986; Horrocks *et al.*, 1999; Burton *et al.*, 2000; Delmelle *et al.*, 2002; Duffell *et al.*, 2001]; however, relatively little attention has been focused on characterization of diffuse degassing from the flanks of Masaya, which, in the case of CO₂, may be a significant contribution to total volcano emissions [St-Amand, 1998; Pérez *et al.*, 2000; Lewicki *et al.*, 2003a].

The study area adjacent to Comalito is characterized by steam emissions through porous and highly fractured lavas and scoria. Soils here are poorly developed with little

vegetation growth. Anomalously high soil temperatures (up to 80°C) and F_{CO_2} (up to $5.0 \times 10^4 \text{ g m}^{-2}\text{d}^{-1}$) of deep magmatic/metamorphic origin have been observed within or around the area [Lewicki *et al.*, 2003a]. Spatial trends in, and correlation between soil gas flux and temperature are consistent with advective transport of heat and CO_2 with steam along a highly permeable fault and/or fault-related fractures [Lewicki *et al.*, 2003a]. A map of F_{CO_2} measured by Group 5 (see Methods section) from 27 to 28 March, 2003 in the area surrounding the study site shows elevated F_{CO_2} on the crater rim of Comalito, along a northwest-trending zone in the immediate vicinity of the study site, and southwest of the study site. (Figure 2). The total CO_2 emission rate from this area ($38,097 \text{ m}^2$) was estimated to be 20.2 ± 2.16 metric tons per day (hereafter referred to as t d^{-1}).

Figure 2.

Methods

Field Measurements

Soil CO_2 flux measurements were made by five groups (Groups 1-5) using the accumulation chamber (AC) method whereby an open-bottomed AC was placed directly on the soil surface, the contained air was circulated through the AC and an infrared gas analyzer (IRGA), and CO_2 concentration ($[CO_2]$) was recorded. Water was removed from the air with $Mg(ClO_4)_2$ or molecular sieve desiccant before the air entered the IRGA. Groups 1-4 calculated F_{CO_2} according to

$$F_{CO_2} = \left(\frac{\rho V}{A} \right) \left(\frac{d[CO_2]}{dt} \right) \quad (1)$$

where ρ is the molar density of air, V is the system volume, A is the AC footprint area, and $d[CO_2]/dt$ is the initial rate of change of $[CO_2]$ in the AC after the AC is placed on the soil surface. All groups report F_{CO_2} in units of $g\ m^{-2}day^{-1}$. In a laboratory setting, *Chiodini et al.* [1998] measured CO_2 flux values within 15% of the imposed flux, whereas *Evans et al.* [2001] recognized a systematic underestimation of flux (average of -12.5%) over an imposed flux range of 200 to 12,000 $g\ m^{-2}d^{-1}$. In a field test, *Carapezza and Granieri* [2004] made repeat F_{CO_2} measurements at two sites with medium (average = 997 $g\ m^{-2}d^{-1}$) and low (average = 5.7 $g\ m^{-2}d^{-1}$) F_{CO_2} and found measurement uncertainties of $\pm 12\%$ and 24% for the medium and low F_{CO_2} sites, respectively.

Group 5 conducted laboratory experiments prior to field measurements to assess the factor (cf) to convert the measured $d[CO_2]/dt$ ($g\ m^{-3}d^{-1}$) to F_{CO_2} ($g\ m^{-2}d^{-1} = g\ m^{-3}d^{-1} \times cf$). A "synthetic soil" was constructed of dry sand (10 cm thick) inside a plastic box with an open top and a range of CO_2 fluxes (90 to 5000 $g\ m^{-2}d^{-1}$) were imposed through this soil using pure CO_2 . Several measurements were made at each imposed flux. The best-fit line to the imposed CO_2 flux versus measured $d[CO_2]/dt$ was determined by linear regression and the slope of this line (i.e., cf) was 0.1345 m. This value was higher than the cf determined theoretically (0.1188 m) for the flux instrumentation used [*Chiodini et al.*, 1998], indicating that the real measurement deviates in some way from the theoretical one. This discrepancy may in part explain the

systematic underestimation of F_{CO_2} by the AC method reported by *Evans et al.* [2001].

The IRGA model and measurement range, A , and V varied between Groups 1-5 (Table 1). Also, Groups 1-4 used WEST Systems Fluxmeters [<http://www.westsystems.com>], whereas Group 5 used a custom-built portable AC measurement system [<http://ipf.ov.ingv.it>]. With the exception of Group 4, all groups either calibrated their IRGA with zero and span gases or checked their IRGA for accuracy using a standard gas within several days before field measurements on Masaya on 27 March, 2003.

Table 1.

Thirty-six F_{CO_2} measurement locations were sited on evenly spaced (5 m) points within a 30x30 m grid using a compass and tape measure. At each grid point, Groups 1-5 sequentially made a F_{CO_2} measurement within the same footprint area within a few minutes of each other. The entire measurement grid was completed by all groups between 10:00 and 13:00 (hereafter referred to as AM measurement time). The measurement grid was repeated by Groups 1-3 between 14:00 and 16:00 (hereafter referred to as PM measurement time).

Data Analysis

To compare the mean F_{CO_2} and total CO_2 emission rate associated with each of the F_{CO_2} data sets measured by Groups 1-5, we chose to apply a single simple statistical method (see Arithmetic Mean section below) to all of the data sets. In addition, to compare the different geostatistical estimation methods, we applied a range of these methods to a single F_{CO_2} data set (the Group 1 AM data set).

Arithmetic Mean The arithmetic mean is the preferred method to estimate the mean of a normally distributed population and has the advantage that it is easy to calculate. However, the arithmetic mean can be sensitive to high data values and does not have the smallest variance when the underlying distribution is lognormal [e.g., *Gilbert, 1987*]. The arithmetic mean and standard deviation were calculated for the F_{CO_2} data sets measured by Groups 1-5. Also, the standard error of the mean was calculated for each data set by dividing the standard deviation by the square root of the sample number. To estimate the total CO₂ emission rate from the study area for each data set, the arithmetic mean F_{CO_2} was multiplied by the grid area (900 m²).

Minimum Variance Unbiased Estimators The *W* test of *Shapiro and Wilk* [1965] was used to determine the underlying distribution of the Group 1 AM data set and results show within a 95% confidence interval that the data are lognormally distributed. Therefore, minimum variance unbiased (MVU) estimators [e.g., *Finney, 1941; Sichel, 1952; Gilbert, 1987*] were used to estimate the mean and variance of the Group 1 AM log-transformed F_{CO_2} data set (Appendix A1). The advantages of using MVU estimators on positively skewed data are that they yield both a statistically unbiased estimate of the mean F_{CO_2} and the smallest variance of unbiased estimators of F_{CO_2} [e.g., *Gilbert, 1987*]. This approach is therefore generally preferred over calculation of the arithmetic mean when the data are positively skewed. To estimate the total CO₂ emission rate from the study area based on the Group 1 AM data set, the MVU mean F_{CO_2} was multiplied by the grid area.

Multiquadric Radial Basis Function In many cases (e.g., when sampled data are unevenly or widely spaced), it is desirable to estimate the value of a variable at unsampled locations within an area of interest. The multiquadric radial basis function method (RB) of interpolation [e.g., *Hardy, 1971; Watson, 1992*] produces a surface that is a combination of a set of circular hyperboloids, each of which is centered on a sampled point (see Appendix A2 for equations). RB tends to interpret small data sets (<250 observations) well and produces a smooth surface that remains faithful to the original sample data. One disadvantage of RB is that boundary effects can produce errors at the edge of the interpolated surface [*Fornberg et al., 2002*]. RB was used to interpolate F_{CO_2} values at one-m spacing in the study area based on the Group 1 AM data set and these values were plotted as an image map using Surfer [*Golden Software, Golden, Colorado*]. The arithmetic mean and standard deviation of the F_{CO_2} estimates were calculated. The total CO₂ emission rate was estimated by multiplying each F_{CO_2} value by 1 m² and summing these products.

Kriging Ordinary kriging (OK) allows F_{CO_2} values to be estimated at unsampled locations as a weighted linear combination of neighboring observations (see Appendix A3 for equations). OK is an unbiased estimator and aims to minimize the estimation variance. OK was used to interpolate F_{CO_2} values at one-m spacing in the study area based on the Group 1 AM data set using Surfer. For consistency between the following geostatistical methods (OK, multi-Gaussian kriging, and sequential Gaussian simulation), the program GSLIB [*Deutsch and Journel, 1998*] was used to calculate all experimental semivariograms for the Group 1 AM data set and model them. For OK,

the experimental semivariogram was calculated using the measured F_{CO_2} values and a spherical model (Appendix A3) was fit to the data (Figure 3a). F_{CO_2} values were then estimated at unsampled locations using OK and the modelled semivariogram values and plotted as an image map using Surfer. The arithmetic mean and standard deviation of the F_{CO_2} estimates were calculated. The total CO₂ emission rate was calculated by multiplying each F_{CO_2} value by 1 m² and summing these products.

Figure 3.

Prediction performances of OK may be better when the sample histogram is normally distributed [e.g., *Saito and Goovaerts, 2000*]. Multi-Gaussian kriging (MGK) was therefore applied to the Group 1 AM data set to interpolate F_{CO_2} values at one-m spacing over the study area. The F_{CO_2} distribution was normalized by performing a normal-score transform using GSLIB. An experimental semivariogram was calculated based on the F_{CO_2} normal scores and a spherical model was fit to the data using GSLIB (Figure 3b). The normal-score F_{CO_2} values were estimated at unsampled locations by OK using Surfer. The normal-score F_{CO_2} estimates were then back-transformed into F_{CO_2} estimates by applying the inverse of the normal-score transform using GSLIB and were plotted as an image map. The arithmetic mean and standard deviation of the F_{CO_2} estimates were calculated. The total CO₂ emission rate was calculated by multiplying each F_{CO_2} value by 1 m² and summing these products.

Sequential Gaussian Simulation A stochastic simulation procedure based on a sequential Gaussian simulation algorithm (sGs) from GSLIB [*Deutsch and Journel, 1998*] was used to map F_{CO_2} and to estimate the total CO₂ emission rate from the study area for the Group 1 AM F_{CO_2} data set, following the approach described by

Cardellini et al. [2003]. The stochastic simulation generates a set of equiprobable representations (realizations) of the spatial distribution of an attribute (e.g., F_{CO_2}) that reasonably reproduces the global statistic and spatial features of the data samples (i.e., the sample histogram and semivariogram model). This technique thus differs from methods (e.g., kriging) which produce a single representation of the attribute's spatial distribution and yield the minimum error variance at each location [*Deutsch and Journel*, 1998]. Moreover, differences among many realizations can be used as a measure of the uncertainty of the attribute estimation [*Goovaerts*, 2001; *Cardellini et al.*, 2003].

SGs operates by considering F_{CO_2} as the realization of a stationary multivariate Gaussian random function. F_{CO_2} is simulated at locations defined by a grid covering the area of interest. The simulation is conditional and sequential (i.e., F_{CO_2} is simulated at each unsampled location by random sampling of a Gaussian conditional cumulative distribution function defined on the basis of the original data and previously simulated data within its neighborhood, as the computation proceeds). Because the sGs procedure requires a multi-Gaussian distribution, a non-normally distributed F_{CO_2} data set is transformed into a normal distribution by a normal-score transform [*Deutsch and Journel*, 1998]. The transformed data are then used in the simulation procedure. Based on the semivariogram model of normal scores, simple kriging is used to estimate F_{CO_2} and the associated variance at each location. The estimate and variance are then used to define a Gaussian conditional cumulative distribution function at each location. A random value is drawn from the conditional cumulative distribution as one "reasonable" simulated value for that location. This value is then added to the data set and can be

used together with the original data to estimate the variable at the next location within the grid. The simulation proceeds to the next grid location and loops until all nodes are simulated. The simulated normal scores are then back-transformed by applying the inverse of the normal-score transform [Deutsch and Journel, 1998]. N alternative simulations are performed and N equiprobable realizations are drawn by changing the starting location of the simulation procedure and thus changing the random path of grid nodes visited. Each of these realizations honors the sampled data at their locations and reproduces the univariate statistics and bivariate properties of the data, within reasonable ergodic fluctuations [Deutsch and Journel, 1998; Cardellini et al., 2003].

Based on the Group 1 AM data set, one-hundred simulations were conducted. The total CO₂ emission rate from the study area was calculated for each realization by multiplying the simulated F_{CO_2} value for each grid cell by 1 m² and summing these products. The mean and standard deviation of the total CO₂ emission rates simulated for N realizations are assumed to be the characteristic CO₂ emission rate for the study area and its uncertainty, respectively. The set of realizations is also used to produce a map of the F_{CO_2} values "expected" at the grid cells (E-type estimates) using a point-wise linear average of all of the realizations.

Results

Comparison of Soil CO₂ Flux Data Sets

F_{CO_2} values measured by Groups 1-5 during AM and PM times range from 218 to 14,719 g m⁻²d⁻¹ (Table 2). Based on the *W* test [*Shapiro and Wilk, 1965*], the data are lognormally distributed within a 95% confidence interval. Skewed distributions are also observed on a histogram of F_{CO_2} measured by Groups 1-5 during AM time (Figure 4).

Table 2.

Figure 4.

The five measurements made by Groups 1-5 at each grid point show that the variability of F_{CO_2} increases with increasing arithmetic mean (Figure 5), and ranges from ± 5 to 167%. To compare the F_{CO_2} data sets measured by Groups 1-5, the mean and variability of each data set was estimated by calculation of the arithmetic mean and standard deviation (Table 2). The total CO₂ emission rates were then estimated by multiplying the arithmetic mean of each group's F_{CO_2} population by the measurement area (900 m²). For the AM measurement time, arithmetic means of F_{CO_2} data sets ranged from 1509 to 2425 g m⁻²d⁻¹, with corresponding total CO₂ emission rates of 1.36 to 2.18 tons d⁻¹. To assess the variability of the estimated F_{CO_2} means and associated total CO₂ emission rates between the different groups' data sets, we calculated the arithmetic mean and standard deviation of the arithmetic means (or emission rates) for the AM data sets measured by Groups 1-5. The arithmetic means and associated emission rates vary by $\pm 22\%$ between the different groups. From AM to PM measurement times, arithmetic means of F_{CO_2} data sets increased from 1607 to 1618 g m⁻²d⁻¹ (total CO₂ emission rates = 1.45 to 1.46 tons d⁻¹) for Group 1, from

Figure 5.

1509 to 1803 $\text{g m}^{-2}\text{d}^{-1}$ (total CO_2 emission rates = 1.36 to 1.62 tons d^{-1}) for Group 2, and from 1767 to 1915 $\text{g m}^{-2}\text{d}^{-1}$ (total CO_2 emission rates = 1.59 to 1.72 tons d^{-1}) for Group 3. In addition, the standard deviation of F_{CO_2} data sets measured by Groups 1-3 consistently increased from AM to PM times.

Figures 6a-c show that there is a near one-to-one relationship between F_{CO_2} measurements made by Groups 1-3 from AM to PM times; however, the slopes of the best-fit lines to these data are consistently >1 (1.1 to 1.2). Measurements made in the AM are moderately correlated ($C = 0.65$) with those made in the PM by Group 1 (Figure 6a), while those made in the AM are well correlated ($C = 0.84$ and 0.82) with those made in the PM by Groups 2 and 3 (Figures 6b and c). During the AM time (Figures 6d-f), measurements made by Groups 1-3 are well correlated ($C=0.75$ to 0.89) with each other. During the PM time, (Figures 6g-i), Group 1-3 measurements are similarly well correlated ($C=0.85$ to 0.95) with each other. Groups 1-3 measured their highest F_{CO_2} at the same grid point in the PM. Also, the second highest F_{CO_2} measured by Groups 1 and 2 and the fourth highest F_{CO_2} measured by Group 3 were measured at the same grid point in the PM. The locations of the two highest fluxes measured by Groups 1 and 2 are also the location of the highest temporal change in flux measured by these groups.

Figure 6.

Figures 7a-f show maps of F_{CO_2} measured by Groups 1-3 during the AM and PM times where each 25 m^2 area represents a F_{CO_2} measurement made in the center of the area. Maps a-f are arranged sequentially in terms of measurement time and the time elapsed between maps ranges from several minutes (between maps a-c and maps d-f)

Figure 7.

to several hours (between maps c and d). The spatial distribution of F_{CO_2} is generally consistent between the different maps. For example, regions of relatively high F_{CO_2} are located in the lower and upper left-hand corners of all maps. The upper left-hand area shows increasing F_{CO_2} from the Group 1 AM to the Group 3 PM measurement times (Figures 7a-f), and the lower left-hand area shows increasing F_{CO_2} from the Group 1 AM to the Group 1 PM measurement times (Figures 7a-d), then F_{CO_2} decreases from the Group 1 to Group 3 PM measurement times (Figures 7d-f).

Comparison of Geostatistical Methods

The means determined using arithmetic and MVU estimators on the raw Group 1 AM data set and the arithmetic means of data sets interpolated/simulated using RB, OK, and sGs are similar (Table 3). To gain an understanding of how the estimated F_{CO_2} means and associated total CO₂ emission rates vary between these methods, we calculated the arithmetic mean and standard deviation of the means (or emission rates). The estimated means and associated total CO₂ emission rates vary between the methods by only $\pm 1.1\%$. The arithmetic mean of the data set interpolated by MGK is relatively low (Table 3), and when MGK is considered, the estimated means and associated total CO₂ emission rates vary between all methods by $\pm 8.0\%$. The standard deviation of the raw Group 1 AM data set ($\pm 1401 \text{ g m}^{-2}\text{d}^{-1}$) is greater than the standard deviation estimated using MVU estimators ($\pm 1376 \text{ g m}^{-2}\text{d}^{-1}$). OK and MGK yield the smallest standard deviations (± 963 and $809 \text{ g m}^{-2}\text{d}^{-1}$, respectively) of all geostatistical methods applied to raw and interpolated data sets.

Table 3.

Figure 8a shows an uninterpolated image map of F_{CO_2} data measured by Group 1 during the AM time. In this map, each 25 m² area represents a F_{CO_2} measurement made in the center of the area. For comparison, each of the statistical interpolation methods was used to construct a map of F_{CO_2} at 1-m spacing based on the Group 1 AM data set (Figures 8b-e). All maps display the same general spatial trends in F_{CO_2} within the study area, with the area of highest F_{CO_2} located in the lower left-hand corner of the maps. Maps interpolated by RB and OK display the smoothest and most continuous spatial variations in F_{CO_2} , while the map simulated using sGs shows the most spatially heterogeneous distribution of F_{CO_2} . Also, the RB and sGs maps preserve the highest and lowest measured F_{CO_2} values, while the OK and MGK maps "dampen" the extreme values.

Figure 8.

Discussion and Conclusions

Sources of Variability of F_{CO_2} Measurements

The arithmetic mean F_{CO_2} and associated total CO₂ emission rate varies by $\pm 22\%$ between Groups 1-5 AM measurements. This variability may be due to measurement error and/or natural change in CO₂ emissions from the study area over time. In addition, the variability of F_{CO_2} measurements made by Groups 1-5 at each grid point ranges from ± 5 to 167%. The trend of increasing variability of measured F_{CO_2} values as the mean F_{CO_2} increases may be due to greater measurement error and/or natural temporal variability of gas flow through the system at relatively high F_{CO_2} . While it

is difficult to separate these effects in a field environment where true F_{CO_2} is unknown and varies with time, measurements made by Groups 1-3 during AM and PM times can be compared to look for consistency within each group's, and between different group's data sets to better understand whether high measurement variability is due in greater part to measurement error or to natural temporal variability of the system.

The slopes of the lines fit to PM versus AM measurements for Groups 1-3 consistently suggest an increase in F_{CO_2} over this time (Figures 6a-c). Because the several highest F_{CO_2} values measured by Groups 1-3 were measured during the PM time at the same grid locations, it appears that these values reflect true F_{CO_2} and are not artifacts of the individual group's measurement methodology. Furthermore, the good correlation observed between measurements made by Groups 1-3 from AM to PM times (Figures 6a-c) and between the different groups measurements during either AM or PM times (Figures 6d-i) indicate good consistency within each group's, and between the different group's, measurements and measurement methodologies. Spatially consistent F_{CO_2} measurements made between Groups 1-3 over time are also reflected in the time series of flux maps (Figures 7a-f). Therefore, based on the 1) consistent increase in average F_{CO_2} measured by Groups 1-3 from AM to PM times, 2) the consistent locations and times of high F_{CO_2} measured by Groups 1-3, 3) the good correlation of measurement made between the different groups, and 4) the spatially consistent changes in F_{CO_2} maps observed over time, we suggest that the high variability of F_{CO_2} observed at relatively high F_{CO_2} is due in large part (although likely not entirely) to natural temporal changes in gas flow through the system, rather than measurement error. It is also likely that the

increase in average F_{CO_2} measured by Groups 1-3 from AM to PM time reflects a true increase in F_{CO_2} from the study area over this time period.

Overall, our results highlight the sensitivity of high F_{CO_2} values to large temporal fluctuations over short time scales. The time series of F_{CO_2} maps we present for Groups 1-3 (Figure 7) capture changes in F_{CO_2} over very short time scales (minutes to hours). To the best of our knowledge, these are the shortest time scales captured to date in repeat measurements of F_{CO_2} grids. These fluctuations are likely due in large part to effects of meteorological parameters on advective gas flow through highly permeable pathways (e.g., fractured lavas and scoria). Wind speed and direction can display large fluctuations over relatively short time scales (i.e., seconds to minutes), whereas atmospheric pressure and temperature typically display large fluctuations over longer time scales. Also, wind speed and F_{CO_2} have been observed to be correlated at short time lag between measurements of these parameters, suggesting that F_{CO_2} may respond rapidly to changes in wind speed [e.g., *Lewicki et al.*, 2003b]. The influence of rapidly fluctuating wind speed and direction on soil gas flow may therefore account for the large variations observed in F_{CO_2} within the study area over relatively short time periods.

Interestingly, F_{CO_2} measurements made by Group 1 during the AM time are moderately correlated with their PM measurements (Figure 6a), while there is higher correlation of measurements from AM to PM times for Groups 2 and 3 (Figures 6b and c). In addition, there is improved correlation of Group 1 measurements with those of Groups 2 and 3 in the PM relative to the AM time (Figures 6d, e, g, and h). Group 1 made the first F_{CO_2} measurements on 27 March, 2003. It is therefore likely that the

highest degree of disturbance of soil and gas flow through this soil during the survey time was caused by Group 1 as they created a new measurement footprint for the AC at each grid location. *Gerlach et al.* [2001] demonstrated that surface disturbances can dramatically alter measured F_{CO_2} . The initial soil disturbance by Group 1 during the AM time may account for the lower degree of correlation observed within Group 1 from AM to PM times relative to the correlation of measurements within Groups 2 and 3, as well as the improved correlation of Group 1 measurements with those of Groups 2 and 3 from AM to PM times. While it is impossible to entirely avoid disturbance of the soil when using the AC technique, precautions should be taken to minimize this disturbance. For example, researchers should wait for an appropriate amount of time following disturbance of the soil until F_{CO_2} measurements are made. Furthermore, the influence of soil disturbance on F_{CO_2} measurements should be considered in interpretations of these measurements.

Sources of variability of F_{CO_2} estimates and maps

The means of the Group 1 AM F_{CO_2} data set and associated total CO₂ emission rates estimated by the different geostatistical methods we present compare well (i.e., vary by only $\pm 1.1\%$), with the exception of those estimated by MGK, which are lower. *Gerlach et al.* [2001] found that kriging models are not seriously distorted by the lack of normal F_{CO_2} distributions. Our results show that the arithmetic mean of the OK interpolated data set compares well to the means of the data sets interpolated using the RB and sGs methods and to the arithmetic mean and MVU estimated mean of

the raw uninterpolated data set. These results suggest that OK has performed well as an estimator when applied to a lognormal distribution. However, the relatively low arithmetic mean of the data set interpolated by MGK suggests that MGK as implemented here does not perform well as an estimator of a lognormal distribution (i.e., has produced underestimates of F_{CO_2}). This is likely due to our application of the inverse of the normal-score transform following kriging of the normal-scored data set, which can lead to a biased estimate of F_{CO_2} [e.g., *Deutsch and Journel, 1998; Saito and Goovaerts, 2000*].

Since the variability of the means and total CO₂ emission rates of a single F_{CO_2} data set estimated using a range of geostatistical methods ($\pm 1.1\%$) is much less than the variability of the arithmetic means of the Groups 1-5 AM data sets ($\pm 22\%$), it may be more important to assess the influences of natural fluctuations of gas flow and/or measurement error on these estimates than it is to assess discrepancies introduced by geostatistical methods. It should be noted, however, that while the mean F_{CO_2} and associated emission rate estimated using the different geostatistical methods compare well, these methods were applied to data collected along a regularly spaced grid. The effects of spatial clustering of measurements on estimates made by different geostatistical methods were therefore not tested in this study and should be considered in future comparative investigations. Also, while sGs yields a total CO₂ emission rate estimate similar to other techniques, it provides the benefit of a measure of the uncertainty associated with this estimate, whereas the other methods considered here do not. This is an important benefit if diffuse CO₂ emissions are to be used to monitor volcanic

activity.

While the differences between the total CO₂ emission rates estimated by the range of geostatistical methods we consider are relatively small, there are important distinctions between the F_{CO_2} maps produced by these methods. For comparison, we present an uninterpolated map of the Group 1 AM F_{CO_2} (Figure 8a). Although it is valuable to first visualize a raw data set without geostatistical interpolation, it is unlikely that a single "point" F_{CO_2} measurement is representative of an entire 25 m² area. In other words, we expect a higher degree of spatial heterogeneity of F_{CO_2} within this area due to the heterogeneous nature of the medium. For example, *Lewicki et al.* [2003a] presented F_{CO_2} measured along profile lines at one-m spacing near our study area and showed a high degree of variability of F_{CO_2} on this small spatial scale (Figure 9).

Figure 9.

As a result, it is necessary to interpolate F_{CO_2} at smaller spatial intervals than at which our measurements were made. The F_{CO_2} map produced by OK is locally accurate and smooth and is therefore appropriate for visualizing general spatial trends in the data. However, OK is likely inappropriate for gas flow modelling where extreme F_{CO_2} values and spatial heterogeneity of F_{CO_2} are important to consider. In our example, RB preserves the extreme measured F_{CO_2} values, but it also yields a F_{CO_2} surface that is smooth and continuous and likely not representative of gas flow through the heterogeneous medium at our study site [*Lewicki et al.*, 2003a]. Relative to OK and RB, sGs produces a spatially heterogeneous distribution of F_{CO_2} . sGs honors the sample histogram and the spatial variability of the data and in this way, it produces the most realistic representation of the spatial distribution of F_{CO_2} .

Appendix A: Data Analyses

A1. MVU Estimators

The mean of the lognormal distribution was estimated using the MVU estimator $\hat{\mu}$ according to

$$\hat{\mu} = \exp\left(\bar{y} + \frac{s_y^2}{2}\right) \quad (\text{A1})$$

where \bar{y} is the arithmetic mean of the n log-transformed values y_i , calculated according to

$$\bar{y} = \frac{1}{n} \sum_{i=1}^n y_i \quad (\text{A2})$$

and s_y^2 is the variance of the n transformed values, calculated according to

$$s_y^2 = \frac{1}{n-1} \sum_{i=1}^n (y_i - \bar{y})^2 \quad (\text{A3})$$

[e.g., *Gilbert*, 1987]. The variance of the lognormal distribution was estimated using the MVU estimator $\hat{\sigma}$ according to

$$\hat{\sigma} = \hat{\mu}^2 \left[\exp\left(s_y^2\right) - 1 \right] \quad (\text{A4})$$

A2. RB

RB estimates the value $\hat{z}(u)$ at unsampled location u (a vector of spatial coordinates) as a weighted linear combination of multiquadric radial basis functions

associated with surrounding observations:

$$\hat{z}(u) = \sum_{i=1}^n w_i(u) C(u_i - u) \quad (\text{A5})$$

where n is the number of sampled points in the data set,

$$C(u_i - u) = ((u_x - u_{ix})^2 + (u_y - u_{iy})^2 + e^2)^{0.5} \quad (\text{A6})$$

is a basis function of the distance on the x-y plane between u and u_i modified by the arbitrary nonnegative constant e , and w_i is the weight assigned to each basis function [e.g., *Watson*, 1992]. The weights are found through the solution of a system of linear equations:

$$\sum_{j=1}^n w_j(u) C(u_i - u_j) + \mu = z(u_i) \quad i = 1, \dots, n(u) \quad (\text{A7})$$

$$\sum_{j=1}^n w_j(u) = 0 \quad (\text{A8})$$

where μ is the Lagrange parameter to satisfy the condition that the weights sum to zero (Equation A8).

A3. OK

OK estimates the value $\hat{z}(u)$ at unsampled location u (a vector of spatial coordinates) as a weighted linear combination of surrounding observations:

$$\hat{z}(u) = \sum_{i=1}^n w_i(u) z(u_i) \quad (\text{A9})$$

where n is the number of sampled points in the data set, $z(u_i)$ is the value of the sampled point, and w_i is the weight assigned to each sampled point [e.g., *Isaaks and Srivastava*, 1989]. The weights are found through the solution of a system of linear equations:

$$\sum_{j=1}^n w_j(u) \gamma(u_i - u_j) + \mu = \gamma(u_i - u) \quad i = 1, \dots, n(u) \quad (\text{A10})$$

$$\sum_{j=1}^n w_j(u) = 1 \quad (\text{A11})$$

where $\gamma(u_i - u_j)$ is the semivariogram model evaluated at the distance between points i and j and μ is the Lagrange parameter. Constraining the weights to sum to unity (Equation A11) maintains the unbiasedness of the estimator. The spherical semivariogram model equation is

$$\gamma(u_i - u_j) = \begin{cases} 1.5 \frac{u_i - u_j}{a} - 0.5 \left(\frac{u_i - u_j}{a} \right)^3 & \text{if } (u_i - u_j) \leq a \\ s & \text{if } (u_i - u_j) > a \\ n & (u_i - u_j) = 0 \end{cases} \quad (\text{A12})$$

where s , a , and n are the sill, range, and nugget effect, respectively, each determined from the statistical properties of the sampled data [e.g., *Isaaks and Srivastava*, 1989].

Acknowledgments.

J. Lewicki was supported by the U.S. Department of Energy under Contract No. DE-AC03-76SF00098 and NASA grant NA-11318. C. Werner was supported by the GeoNet Project sponsored by the following New Zealand governmental agencies: Earthquake Commission (EQC), Geological and Nuclear Sciences Limited (GNS), and Foundation for Research, Science and Technology (FRST). D. Bergfeld was supported by the U.S. Geological Survey as a National Research Council Post-Doctoral Associate. We acknowledge the Eighth Field Workshop on Volcanic Gases, sponsored by the Commission on the Chemistry of Volcanic Gases and the International Association of Volcanology and Chemistry of the Earth's Interior for the opportunity to make comparative soil CO₂ flux measurements on Masaya volcano. We thank C. Doughty (Lawrence Berkeley National Lab) for constructive review of the manuscript and G.E. Hilley (University of California, Berkeley) for helpful discussions.

References

- Bergfeld, D., F. Goff, and C. J. Janik, Elevated carbon dioxide flux at the Dixie Valley geothermal field, Nevada; relations between surface phenomena and the geothermal reservoir, *Chem. Geol.*, *177*, 43–66, 2001.
- Burton, M., C. Oppenheimer, L. Horrocks, and P. Francis, Remote sensing of CO₂ and H₂O emission rates from Masaya volcano, Nicaragua, *Geology*, *28*, 915–918, 2000.
- Carapezza, M. L., and D. Granieri, CO₂ soil flux at Vulcano (Italy): comparison of active and passive methods, *Appl. Geochem.*, *19*, 73–88, 2004.
- Cardellini, C., G. Chiodini, and F. Frondini, Application of stochastic simulation to CO₂ flux from soil: Mapping and quantification of gas release, *J. Geophys. Res.*, *108*, 2425, 2003.
- Chiodini, G., G. R. Cioni, M. Guidi, B. Raco, and L. Marini, Soil CO₂ flux measurements in volcanic and geothermal areas, *Appl. Geochem.*, *13*, 543–552, 1998.
- Chiodini, G., C. Cardellini, F. Frondini, D. Granieri, L. Marini, and G. Ventura, CO₂ degassing and energy release at Solfatara Volcano, Campi Flegrei, Italy, *J. Geophys. Res.*, *106*, 16,213–16,221, 2001.
- Delmelle, P., J. Stix, P. Baxter, J. Garcia-Alvarez, and J. Barquero, Atmospheric dispersion, environmental effects and potential health hazard associated with the low-altitude gas plume of Masaya volcano, Nicaragua, *Bull. Volcanol.*, *64*, 423–434, 2002.
- Delmelle, P., et al., Origin, effects of Masaya volcano's continued unrest probed in Nicaragua, *Eos (Transactions, American Geophysical Union)*, *80*, 575,581, 1999.
- Deutsch, C. V., and A. G. Journel, *GSLIB, Geostatistical Software Library and Users Guide*, Oxford Univ. Press, New York, 1998.

- Duffell, H., C. Oppenheimer, and M. Burton, Volcanic gas emission rates measured by solar occultation spectroscopy, *Geophys. Res. Lett.*, *28*, 3131–3134, 2001.
- Evans, W. C., M. L. Sorey, B. M. Kennedy, D. A. Stonestrom, J. D. Rogie, and D. L. Shuster, High CO₂ emissions through porous media: transport mechanisms and implications for flux measurement and fractionation, *Chem. Geol.*, *177*, 15–29, 2001.
- Farrar, C. D., M. L. Sorey, W. C. Evans, J. F. Howle, B. D. Kerr, B. M. Kennedy, Y. King, and J. R. Southon, Forest-killing diffuse CO₂ emission at Mammoth Mountain as a sign of magmatic unrest, *Nature*, *376*, 675–678, 1995.
- Finney, D. J., On the distribution of a variate whose logarithm is normally distributed, *J. Royal Statist. Soc. Suppl.*, *7*, 144–161, 1941.
- Fornberg, B., T. A. Driscoll, G. Wright, and R. Charles, Observations on the behavior of radial basis function approximations near boundaries, *Comp. Mathem. Appl.*, *43*, 473–490, 2002.
- Gerlach, T., M. Doukas, K. McGee, and R. Kessler, Soil efflux and total emission rates of magmatic CO₂ at the Horseshoe Lake tree kill, Mammoth Mountain, California, *Chem. Geol.*, *177*, 101–116, 2001.
- Giammanco, S., S. Gurrieri, and M. Valenza, Soil CO₂ degassing along tectonic structures on Mount Etna (Sicily); the Pernicana fault, *Appl. Geochem.*, *12*, 429–436, 1997.
- Gilbert, R. O., *Statistical Methods for Environmental Pollution Monitoring*, Van Nostrand Reinhold, New York, 1987.
- Goovaerts, P., Geostatistical modeling of uncertainty in soil science, *Geoderma*, *103*, 3–26, 2001.

- Hardy, R. L., Multiquadric equations of topography and other irregular surfaces, *J. Geophysics Resour.*, *76*, 1905–1915, 1971.
- Horrocks, L., M. Burton, and P. Francis, Stable gas plume composition measured by OP-FTIR spectroscopy at Masaya Volcano, Nicaragua, 1998-1999, *Geophys. Res. Lett.*, *26*, 3497–3500, 1999.
- Isaaks, E. H., and R. M. Srivastava, *An introduction to applied geostatistics*, Oxford University Press, New York, 1989.
- Lewicki, J. L., C. Connor, K. St-Amand, J. Stix, and W. Spinner, Self-potential, soil CO₂ flux, and temperature on Masaya volcano, Nicaragua, *Geophys. Res. Lett.*, *30*, 1817, 2003a.
- Lewicki, J. L., W. C. Evans, G. E. Hilley, M. L. Sorey, J. D. Rogie, and S. L. Brantley, Shallow soil CO₂ flow along the San Andreas and Calaveras faults, CA, *J. Geophysics Res.*, *108*, 2187, 2003b.
- Pérez, N., J. Salazar, A. Saballos, J. Álvarez, F. Segura, P. Hernández, and K. Notsu, Diffuse degassing of CO₂ from Masaya caldera, Central America, *Eos Trans. AGU, Fall Meet. Suppl.*, *81*, 2000.
- Rogie, J. D., D. M. Kerrick, M. L. Sorey, G. Chiodini, and D. L. Galloway, Dynamics of carbon dioxide emission at Mammoth Mountain, California, *Earth Planet. Sci. Lett.*, *188*, 535–541, 2001.
- Saito, H., and P. Goovaerts, Geostatistical interpolation of positively skewed and censored data in a dioxin-contaminated site, *Env. Sci. Technol.*, *34*, 4228–4235, 2000.
- Salazar, J. M., P. A. Hernández, N. M. Pérez, G. Melián, J. Álvarez, F. Segura, and K. Notsu,

- Diffuse emission of carbon dioxide from Cerro Negro volcano, Nicaragua, Central America, *Geophys. Res. Lett.*, *22*, 4275–4278, 2001.
- Shapiro, S. S., and M. B. Wilk, An analysis of variance test for normality (complete samples), *Biometrika*, *52*, 591–611, 1965.
- Sichel, H. S., New methods in the statistical evaluation of mine sampling, *London Inst. Mining Met. Trans.*, *61*, 261–288, 1952.
- St-Amand, K., The distribution and origin of radon, CO₂, and SO₂ gases and multifractal behavior of SO₂ at Masaya volcano, Nicaragua, Master's thesis, Université de Montréal, 1998.
- Stoiber, R. E., S. N. Williams, and B. J. Huebert, Sulfur and halogen gases at Masaya caldera complex, Nicaragua: total flux and variations with time, *J. Geophys. Res.*, *91*, 12,215–12,231, 1986.
- Wardell, L. J., P. Delmelle, T. Fischer, J. L. Lewicki, E. Malavassi, J. Stix, and W. Strauch, Volcanic gas workshop fosters international focus on state of the art measurement techniques, *Eos (Transactions, American Geophysical Union)*, *84(47)*, 519, 2003.
- Watson, D. F., *Contouring: a guide to the display and analysis of spatial data*, Pergamon, New York, 1992.
- Welles, J. M., T. H. Demetriades-Shah, and D. K. McDermitt, Considerations for measuring ground CO₂ effluxes with chambers, *Chem. Geol.*, *177*, 3–13, 2001.
- Werner, C. A., S. L. Brantley, and K. Boomer, CO₂ emissions related to the Yellowstone volcanic system 2: Statistical sampling, total degassing, and transport mechanisms, *J. Geophys. Res.*, *105*, 10,831–10,846, 2000.

J. L. Lewicki, Earth Sciences Division, Lawrence Berkeley National Laboratory,
Berkeley, California, USA

D. Bergfeld, U.S. Geological Survey, Menlo Park, California, USA

C. Cardellini, Dipartimento di Scienze della Terra, Università di Perugia, Perugia,
Italy

G. Chiodini, Osservatorio Vesuviano, Istituto Nazionale di Geofisica e Vulcanologia,
Naples, Italy

D. Granieri, Osservatorio Vesuviano, Istituto Nazionale di Geofisica e Vulcanologia,
Naples, Italy

N. Varley, Facultad de Ciencias, Universidad de Colima, Colima, Mexico

C. Werner, Institute of Geological and Nuclear Sciences, Taupo, New Zealand

Received _____

This manuscript was prepared with AGU's \LaTeX macros v5, with the extension
package 'AGU++' by P. W. Daly, version 1.6b from 1999/08/19. ENVIRONMENT

Figure Captions

Figure 1. Areal photograph showing study site location adjacent to Comalito cinder cone on the flanks of Masaya volcano. Also shown are the summit Nindiri, San Pedro, Santiago (active), and Masaya craters.

Figure 2. (a) Map of F_{CO_2} within area surrounding the study site (white box) simulated using the sGs method (see Data Analysis section). Map shows mean F_{CO_2} determined by point-wise linear averaging of 300 simulations. White dots show measurement locations. (b) Experimental (dots) and model (line) semivariograms of F_{CO_2} normal scores used in the sGs procedure .

Figure 3. Experimental (dots) and model (line) semivariograms of (a) F_{CO_2} and (b) F_{CO_2} normal scores (Group 1 AM data set). The spherical model parameters are shown.

Figure 4. Histogram of AM F_{CO_2} data sets for Groups 1-5.

Figure 5. Plot of standard deviation (σ) versus arithmetic mean (μ) of F_{CO_2} measured at each grid point during the AM measurement time by Groups 1-5.

Figure 6. Plots of F_{CO_2} measured during PM versus AM times for (a) Group 1, (b) Group 2, and (c) Group 3. Plots of F_{CO_2} measured during AM time by (d) Group 2 versus Group 1, (e) Group 3 versus Group 1, and (f) Group 3 versus Group 2. Plots of F_{CO_2} measured during PM time by (g) Group 2 versus Group 1, (h) Group 3 versus Group 1, and (i) Group 3 versus Group 2. Also shown on each plot are a line (solid) showing one-to-one correlation, the best-fit line (dashed) to data determined by linear regression, the equation for this line, and the correlation coefficient (C) for the data.

Figure 7. Time series of uninterpolated maps of F_{CO_2} measured by Groups 1-3 during AM and PM times. Each 5x5 m area represents a F_{CO_2} measurement. Black dots show measurement locations.

Figure 8. (a) Uninterpolated map of F_{CO_2} measured by Group 1 during AM measurement time. Each 5x5 m square represents a separate F_{CO_2} measurement. Black dots show measurement locations. (b), (c), (d), and (e) Maps of F_{CO_2} for the RB, OK, MGK, and sGs methods, respectively.

Figure 9. Log F_{CO_2} versus distance along a profile line near the study site (modified from *Lewicki et al.* [2003a]). F_{CO_2} measurements made at one-m spacing show a high degree of variability on this spatial scale.

Tables

Table 1. IRGA, A , and V of AC measurement systems used by Groups 1-5.

Group	IRGA model	IRGA range ppmv CO ₂	A m ²	V m ³
1	LI-COR LI-800	0-20,000	$3.2e^{-2}$	$6.3e^{-3}$
2	LI-COR LI-820	0-2000	$3.1e^{-2}$	$6.2e^{-3}$
3	LI-COR LI-820	0-10,000	$3.8e^{-2}$	$2.9e^{-3}$
4	LI-COR LI-800	0-5000	$3.1e^{-2}$	$3.1e^{-3}$
5	LI-COR LI-800	0-20,000	$3.1e^{-2}$	$2.1e^{-3}$

Table 2. F_{CO_2} range, arithmetic mean (μ), standard deviation (σ), standard error of the mean (σ_μ) and total CO₂ emission rate from study area for Groups 1-5.

Group	Measurement time	F_{CO_2} range	μ	σ	σ_μ	CO ₂ emission rate
		g m ⁻² d ⁻¹	g m ⁻² d ⁻¹	g m ⁻² d ⁻¹		ton d ⁻¹
1	AM	299-6905	1488	1401	234	1.34
2	AM	362-7006	1767	1518	253	1.59
3	AM	231-9292	1509	1633	272	1.36
4	AM	218-11,924	2425	3216	536	2.18
5	AM	351-12,277	2188	2398	400	1.97
1	PM	255-14,719	1618	2645	441	1.46
2	PM	341-11,158	1915	2226	371	1.72
3	PM	267-11,134	1803	2319	387	1.62

AM refers to grid measured between 10:00 and 13:00 and PM refers to grid measured between 14:00 and 16:00. Total CO₂ emission rates were calculated by multiplying the measurement area (900 m²) by the arithmetic mean of each F_{CO_2} population.

Table 3. Mean, standard deviation, and total CO₂ emission rate estimated for the Group 1 AM data set using different geostatistical methods.

Method	μ	σ	CO ₂ emission rate
	g m ⁻² d ⁻¹	g m ⁻² d ⁻¹	ton d ⁻¹
Arithmetic	1488	1401	1.34
MVU	1471	1376	1.32
RB	1493	1161	1.34
OK	1492	963	1.34
MGK	1210	809	1.09
sGs	1516		1.36±0.154

The mean F_{CO_2} reported for sGs is the mean of the 100 simulations.

Figures

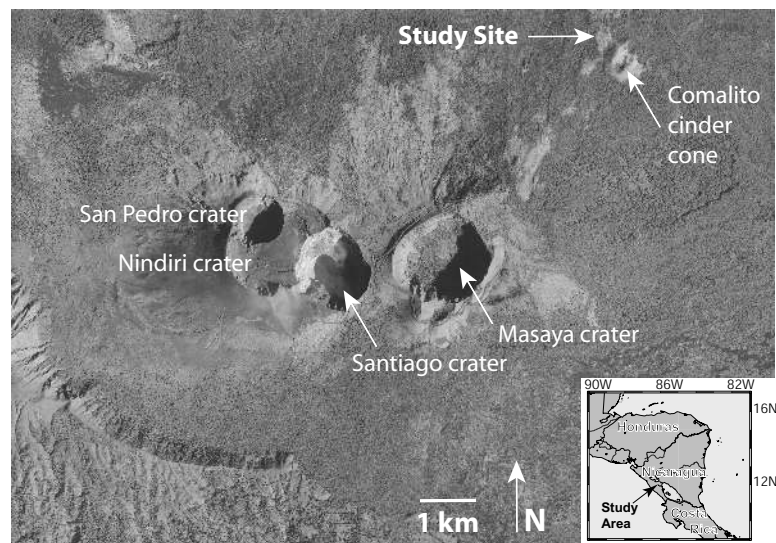


Figure 1. Aerial photograph showing study site location adjacent to Comalito cinder cone on the flanks of Masaya volcano. Also shown are the summit Nindiri, San Pedro, Santiago (active), and Masaya craters.

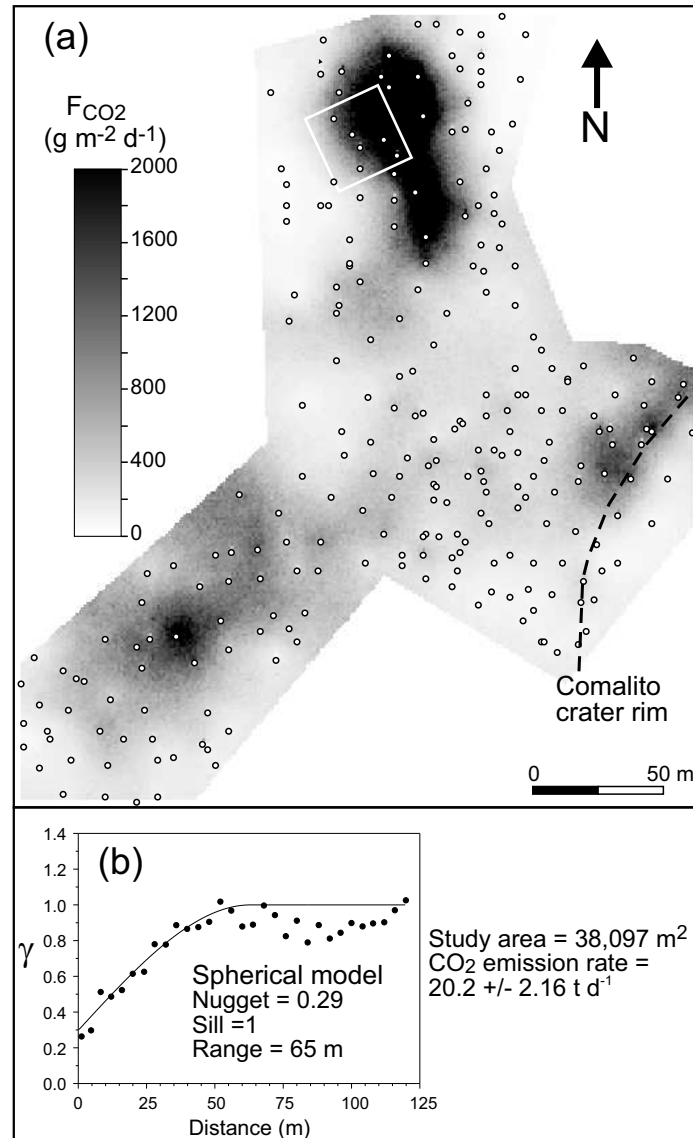


Figure 2. (a) Map of F_{CO_2} within area surrounding the study site (white box) simulated using the sGs method (see Data Analysis section). Map shows mean F_{CO_2} determined by point-wise linear averaging of 300 simulations. White dots show measurement locations. (b) Experimental (dots) and model (line) semivariograms of F_{CO_2} normal scores used in the sGs procedure .

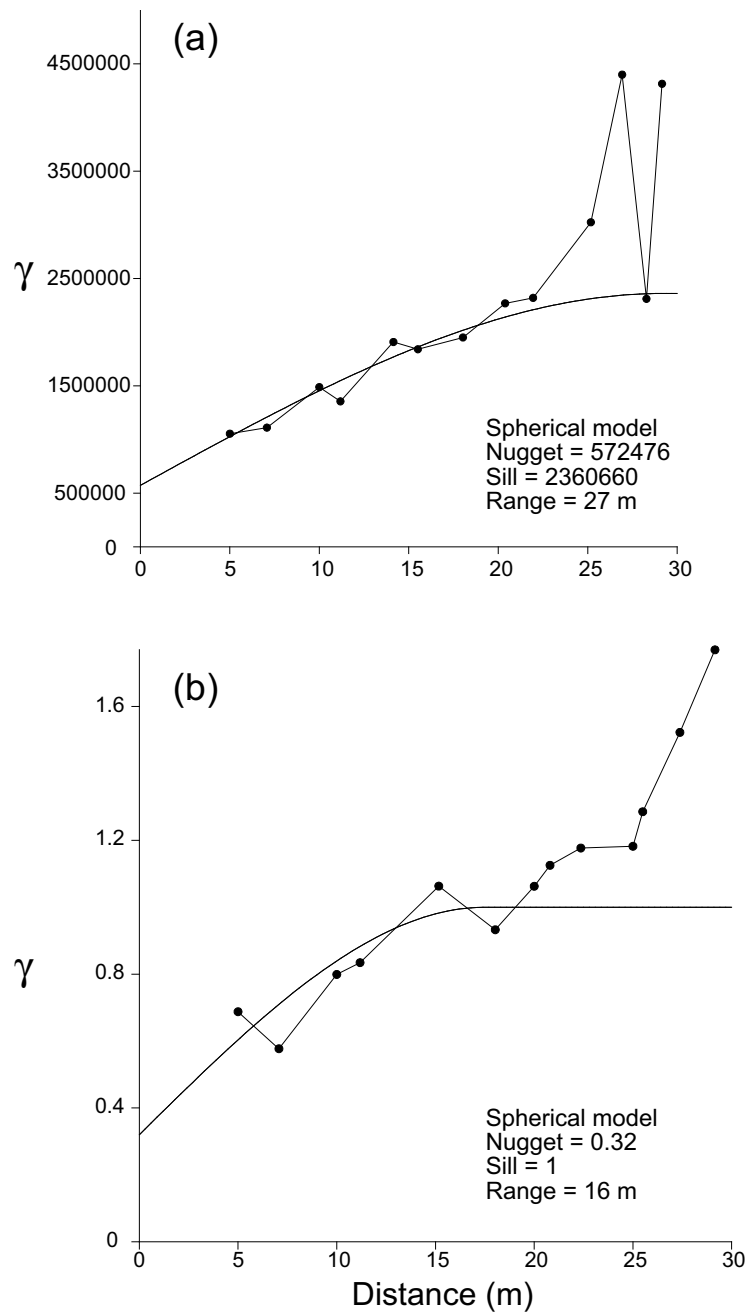


Figure 3. Experimental (dots) and model (line) semivariograms of (a) F_{CO_2} and (b) F_{CO_2} normal scores (Group 1 AM data set). The spherical model parameters are shown.

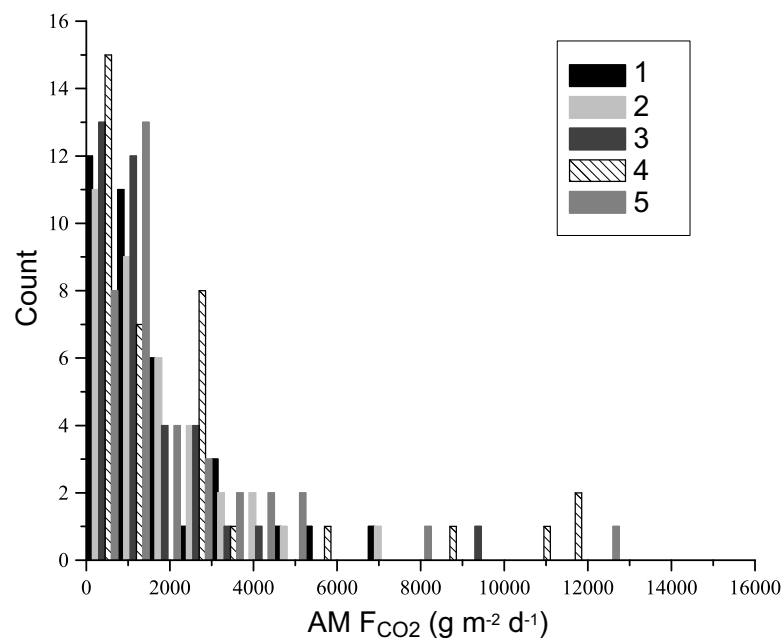


Figure 4. Histogram of AM F_{CO2} data sets for Groups 1-5.

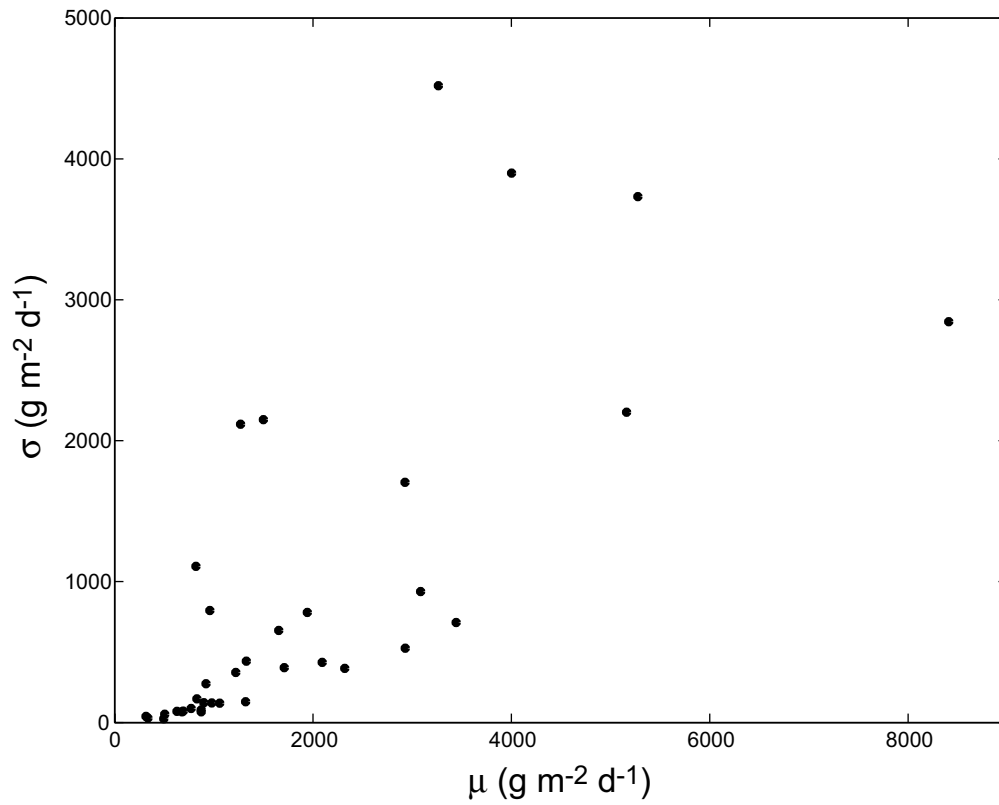


Figure 5. Plot of standard deviation (σ) versus arithmetic mean (μ) of F_{CO_2} measured at each grid point during the AM measurement time by Groups 1-5.

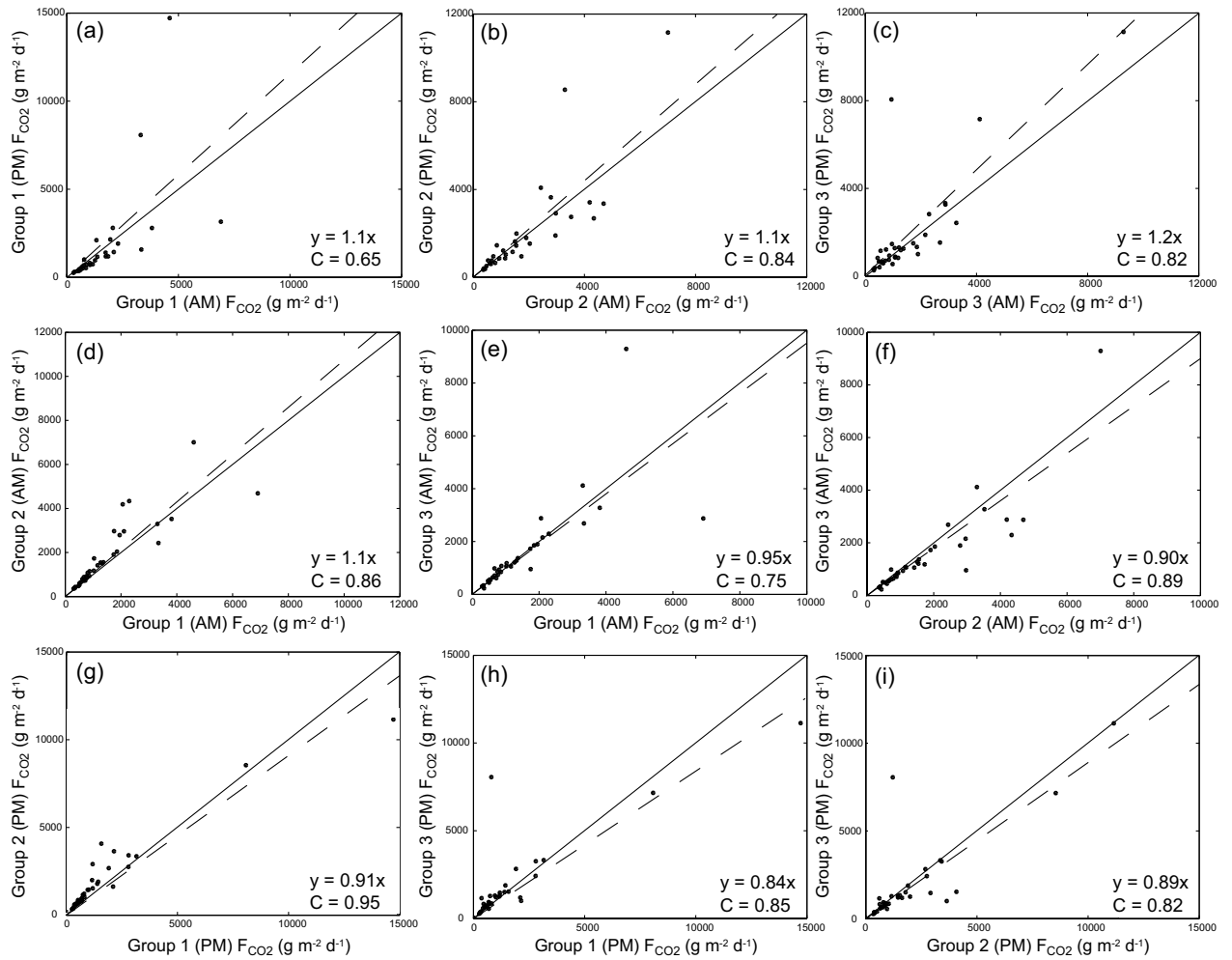


Figure 6. Plots of F_{CO_2} measured during PM versus AM times for (a) Group 1, (b) Group 2, and (c) Group 3. Plots of F_{CO_2} measured during AM time by (d) Group 2 versus Group 1, (e) Group 3 versus Group 1, and (f) Group 3 versus Group 2. Plots of F_{CO_2} measured during PM time by (g) Group 2 versus Group 1, (h) Group 3 versus Group 1, and (i) Group 3 versus Group 2. Also shown on each plot are a line (solid) showing one-to-one correlation, the best-fit line (dashed) to data determined by linear regression, the equation for this line, and the correlation coefficient (C) for the data.

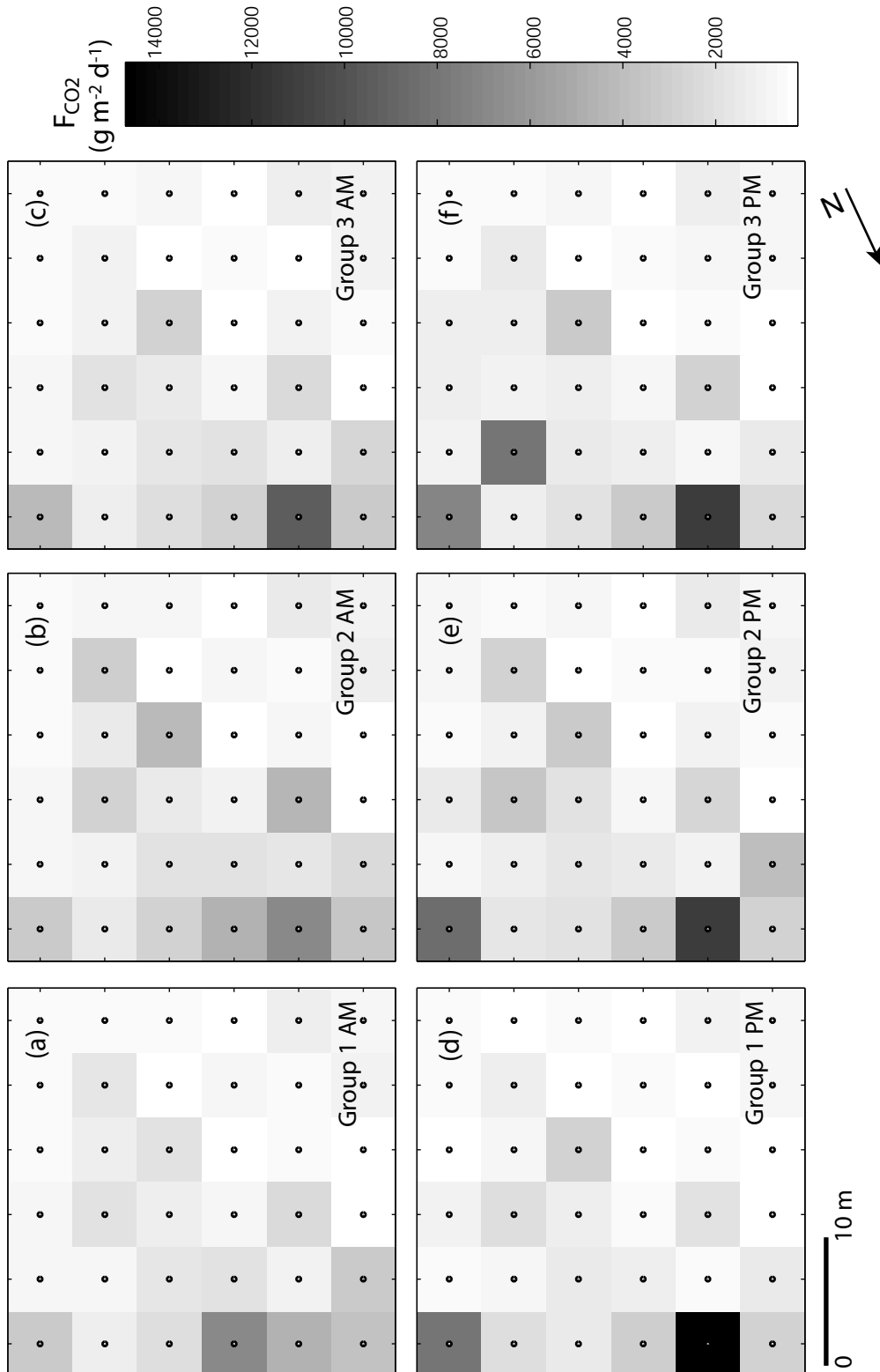


Figure 7. Time series of uninterpolated maps of F_{CO_2} measured by Groups 1-3 during AM and PM times. Each 5x5 m area represents a F_{CO_2} measurement. Black dots show measurement locations.

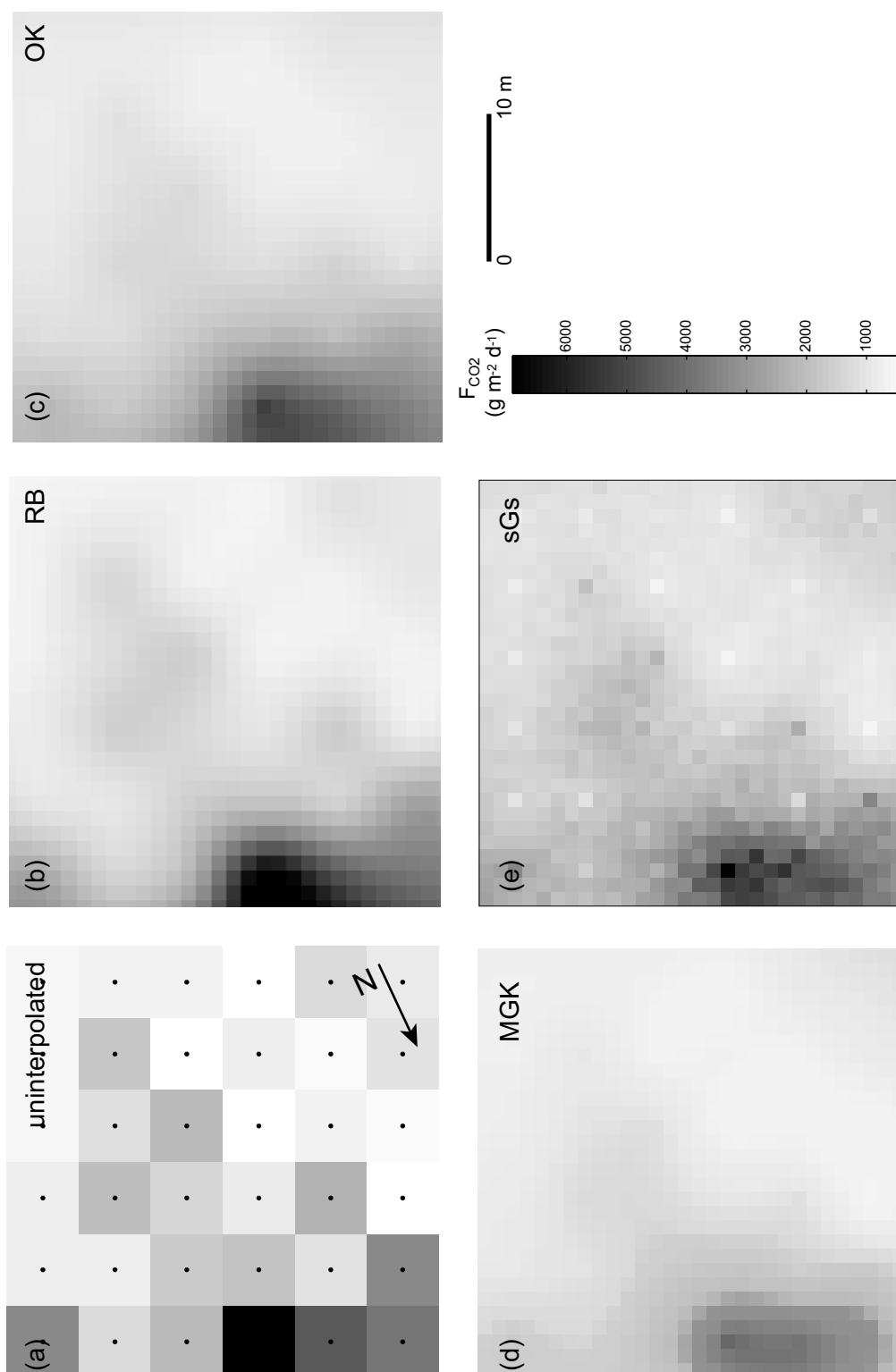


Figure 8. (a) Uninterpolated map of F_{CO_2} measured by Group 1 during AM measurement time. Each 5x5 m square represents a separate F_{CO_2} measurement. Black dots show measurement locations. (b), (c), (d), and (e) Maps of F_{CO_2} for the RB, OK, MGK, and sGs methods, respectively.

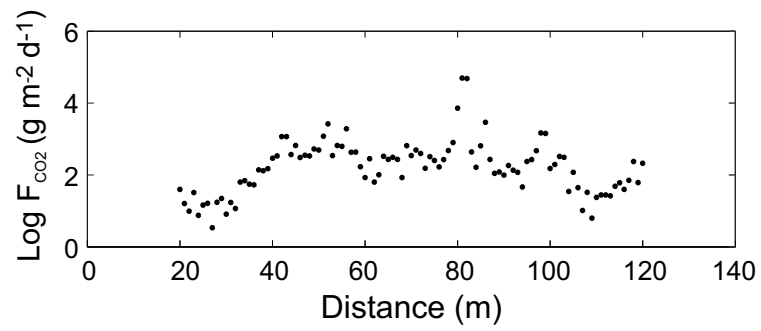


Figure 9. Log F_{CO_2} versus distance along a profile line near the study site (modified from *Lewicki et al.* [2003a]). F_{CO_2} measurements made at one-m spacing show a high degree of variability on this spatial scale.